

Crystal Reorientation and Amorphization Induced by Stressing Efficient and Stable P–I–N Vacuum-Processed MAPbI₃ Perovskite Solar Cells

Ismail C. Kaya, Kassio P. S. Zanoni,* Francisco Palazon, Michele Sessolo, Hasan Akyildiz, Savas Sonmezoglu, and Henk J. Bolink*

Herein, the long-term stability of vacuum-deposited methylammonium lead iodide (MAPbI₃) perovskite solar cells (PSCs) with power conversion efficiencies (PCEs) of around 19% is evaluated. A low-temperature atomic layer deposition (ALD) Al₂O₃ coating is developed and used to protect the MAPbI₃ layers and the solar cells from environmental agents. The ALD encapsulation enables the MAPbI₃ to be exposed to temperatures as high as 150 °C for several hours without change in color. It also improves the thermal stability of the solar cells, which maintain 80% of the initial PCEs after aging for ≈40 and 37 days at 65 and 85 °C, respectively. However, room-temperature operation of the solar cells under 1 sun illumination leads to a loss of 20% of their initial PCE in 230 h. Due to the very thin ALD Al₂O₃ encapsulation, X-ray diffraction can be performed on the MAPbI₃ films and completed solar cells before and after the different stress conditions. Surprisingly, it is found that the main effect of light soaking and thermal stress is a crystal reorientation with respect to the substrate from (002) to (202) of the perovskite layer, and that this reorientation is accelerated under illumination.

1. Introduction

Organic–inorganic lead halide perovskite solar cells (PSCs) have attracted considerable scientific and technological attention over the past decade due to simple fabrication processes and a tremendous increase in power conversion efficiency (PCE) since the first report in 2009.^[1] A typical PSC consists of a transparent conductive oxide (TCO), electron and hole transporting layers (ETL and HTL, respectively), a perovskite film, and a metal electrode.^[2,3] PSCs can be fabricated in two different configurations depending on the order of fabrication starting from the front transparent electrode, either n–i–p (conventional) or p–i–n (inverted).^[4,5] PSCs in the p–i–n configuration usually show less hysteresis in the *J–V* curves and are more suited for flexible and tandem architectures, and recently reached a certified PCE of 22.3%,^[6] which

is close to the record PCEs observed in n–i–p PSCs.^[6–8] Although PSCs have reached encouraging high efficiency in laboratory scale, one of the main issues to be addressed in view of commercialization is the long-term instability.^[9,10] There are many factors that influence the stability of PSCs such as light, heat, oxygen, and moisture in particular when these are combined.^[11–13]

The stability of PSCs depends on many parameters, in particular the device architecture, the selected charge extraction layers, the perovskite composition, and the interaction between them. Of course, one of the primary concerns is the perovskite absorber layer itself. Its composition is a very important factor and until recently pure-MA-based perovskites were considered unstable.^[14,15] Recently, however, Holzhey et al., demonstrated that solution-processed MAPbI₃-based solar cells exhibited operational stability in excess of 500 h under illumination when kept at 65 °C.^[16] It has been found that the residual solvent in the perovskite layer,^[17] crystal structure,^[18] grain size,^[19] defect density,^[20,21] and compactness of the film^[22] affect the degradation of the perovskite layer.^[23] Therefore, the preparation method is an important factor in obtaining stable perovskite films. Perovskite films have been fabricated by several methods, such as spin coating,^[24] spray deposition,^[25] dip coating,^[26] doctor blading,^[27] and vacuum deposition.^[28–30] Among these, vacuum deposition is

I. C. Kaya, Dr. K. P. S. Zanoni, Dr. F. Palazon, Dr. M. Sessolo, Prof. H. J. Bolink
Instituto de Ciencia Molecular
Universidad de Valencia
C/Catedrático J. Beltrán 2, Paterna 46980, Spain
E-mail: kassio.zanoni@uv.es; henk.bolink@uv.es

I. C. Kaya, Dr. H. Akyildiz
Department of Metallurgical and Materials Engineering
Konya Technical University
Konya, Turkey

Dr. S. Sonmezoglu
Department of Metallurgical and Materials Engineering
Karamanoglu Mehmetbey University
Karaman, Turkey

 The ORCID identification number(s) for the author(s) of this article can be found under <https://doi.org/10.1002/aesr.202000065>.

© 2021 The Authors. Advanced Energy and Sustainability Research published by Wiley-VCH GmbH. This is an open access article under the terms of the Creative Commons Attribution License, which permits use, distribution and reproduction in any medium, provided the original work is properly cited.

DOI: 10.1002/aesr.202000065

the only method to produce perovskite films without using any solvent.^[31] Furthermore, this method enables one to form large-area, uniform, and compact films without pinholes.^[32–34]

Using vacuum-assisted thermal cosublimation, our group has in the past developed several fully evaporated PSCs, in both the n–i–p and p–i–n configurations.^[4,35] In particular for the p–i–n PSCs, it was demonstrated that the elimination of the partially oxidized and reduced HTL and ETL from the device stack leads to improvements in the stability. However, there is a significant energy mismatch between the highest occupied molecular orbital (HOMO) of most organic charge transport materials and the work function of indium tin oxide (ITO) used as the transparent electrode in most devices.^[36] Therefore, to ensure efficient charge extraction, a thin interlayer is frequently deposited in between the ITO and the HTL, such as MoO₃, strongly oxidizing molecules, or self-assembled monolayers (SAMs).^[37,38] In addition to these, there are a few single-layer HTLs that lead to efficient charge extraction to the ITO, such as NiO, poly(3,4-ethylenedioxythiophene):polystyrenesulfonate (PEDOT:PSS), and poly[bis(4-phenyl)(2,5,6-trimethylphenyl)amine] (PTAA).^[39,40] Recently, it has been shown that p–i–n PSCs with high efficiency can be manufactured using dopant-free PTAA in the form of very thin films (units of nanometers).^[40–43] Furthermore, Boldyreva et al. reported that dopant-free PTAA is more stable at the perovskite interface than NiO or PEDOT:PSS HTLs.^[44]

There are also external factors that influence the stability of PSCs, such as light, heat, oxygen, and moisture; although the first two remain critical and unavoidable, the last two can be circumvented by proper encapsulation of the device in inert atmosphere gloveboxes right after fabrication.^[12,45] Many types of encapsulation have been tested in PSCs using different shielding materials,^[46] such as ethylene vinyl acetate,^[47] UV-vis curable epoxy resins,^[48,49] polymeric coatings,^[50] adhesives,^[51] and polymer/glass or polymer/metal plate stacks.^[52,53] In special, atomic layer deposition (ALD) of moisture barrier layers is a well-known encapsulation agent in organic light-emitting diodes (OLEDs).^[54] In ALD, ultrathin layers with atomic proportions are obtained by a sequential exposure of the substrate to gas phase precursors, in a self-limited controlled layer-by-layer deposition, enabling dense, pinhole-free inorganic films with high 3D conformality and excellent surface coverage.^[46,55] The use of ALD for encapsulation is particularly interesting for PSCs to diminish the perovskite toxicity effects and their quick degradation in air, as reviewed by Zardetto et al.^[56] Among the many oxides obtainable by ALD, Al₂O₃ is a versatile material that can be ALD-grown from trimethylaluminum (TMA) and water (or ozone) as precursors on top of different materials with all types of hydrophilicity and has a very-low water vapor transmission rate of 10^{−6} g m^{−2} per day.^[46] There are only a few works to report PSC stability improvements using ALD-coated Al₂O₃^[46,57–61] and the main drawbacks lie in the usual aggressive deposition conditions (mostly, the high temperature range typically applied in many ALD protocols, usually from 80 to 300 °C) that can stress and degrade the perovskite underlayer, decreasing the initial pre-encapsulated PSC efficiencies. For example, ALD deposition of Al₂O₃ on MAPbI₃ PSCs usually requires mild conditions (60 °C) to reach stability with no costs to efficiency,^[46,61] yet to date there are no examples of ALD-Al₂O₃ encapsulation for

efficient and stable MAPbI₃-based p–i–n PSCs in which the perovskite is processed by coevaporation.

To obtain information about the stability of vacuum-processed MAPbI₃-based PSCs, we, therefore, selected PTAA as the HTL due to its simplicity compared to other options. To exclude as much as possible the effect of atmosphere,^[62] we developed a low-temperature (40 °C) ALD process to encapsulate the perovskite film and the devices with a thin Al₂O₃ layer. This encapsulation allows heating the MAPbI₃ film up to 150 °C for more than 4 h, without any noticeable degradation. This rigorous encapsulation was also applied to the thin-film solar cells exhibiting PCE > 19%, which increased their thermal shelf stability, at 65 and 85 °C, to 1125 and 875 h, respectively (taken as the time where the PCE dropped to 80% of its initial value, *t*₈₀). However, the operational stability (*t*₈₀) at room temperature and 1 sun AM 1.5 simulated sunlight was limited to 265 h (≈11 days). We found that this decrease in operational stability was not caused by a degradation of the perovskite film but rather to a change in crystal orientation of the perovskite. This important finding implies that when rigorously encapsulated, the perovskite layer does not decompose into its precursors (PbI₂, MAI), but actually changes orientation with respect to the substrate. This effect occurs with temperature, but much faster under intense illumination. The mechanism responsible for this effect is currently being investigated.

2. Results and Discussion

2.1. Characterization of MAPbI₃ on PTAA

Thin MAPbI₃ films were formed by dual-source vacuum deposition of MAI and PbI₂ (with deposition rates of 1 and 0.6 Å s^{−1}, respectively) following the procedure used to obtain high-efficiency solar cells reported elsewhere^[18,63] (see the Experimental Section for more details). Here, the ITO-coated glass substrates were coated with a thin layer of PTAA that was spin coated at 7000 rpm from a toluene solution (1.5 mg mL^{−1}). A representative X-ray diffraction (XRD) pattern of these MAPbI₃ films is given in **Figure 1A**. The pattern can be fitted by taking into account three different materials: tetragonal MAPbI₃, ITO, and PbI₂. The main peaks of ITO and PbI₂ are marked in **Figure 1A**. The whole-pattern fit, including all calculated Bragg's reflections for the three phases, can be found in **Figure S1**, Supporting Information. The small amount of residual PbI₂ impurity present in our films has been observed by others and is considered advantageous to the performance of the PSCs due to its passivation effect on the grain boundaries.^[64] While the calculated cell parameters for MAPbI₃ (see **Table S1**, Supporting Information) are in very close agreement to reference data,^[65] the relative intensities of the diffraction peaks are indicative of a preferential orientation along the *c*-axis (see **Figure 1A** and **Table S2**, Supporting Information). This is the most common orientation of MAPbI₃ thin films prepared either by solution or by vacuum processes.^[66,67]

The microstructural features of the evaporated MAPbI₃ films on PTAA were investigated by a field-emission scanning electron microscope (FE-SEM) and atomic force microscopy (AFM), as shown in **Figure 1**, respectively. The size distribution of the grains is also displayed as an inset in **Figure 1C**. The AFM measurement

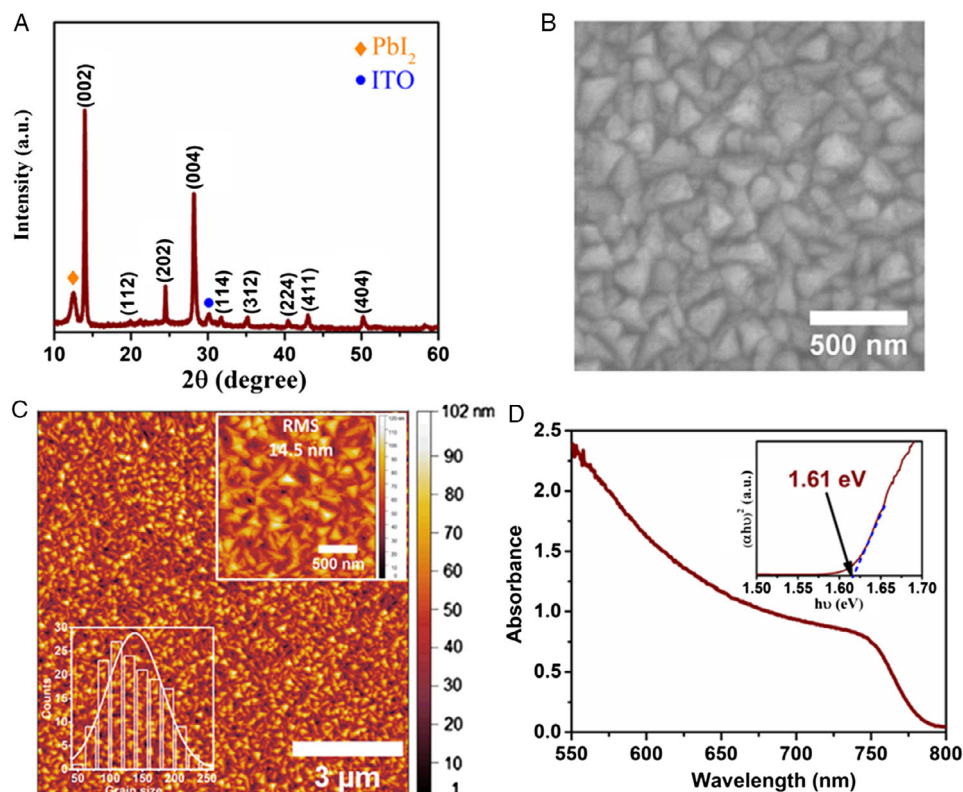


Figure 1. A) XRD pattern, B) FE-SEM image, C) AFM topography, and D) absorbance spectrum of a coevaporated MAPbI₃ film (the insets given in C show the grain size distribution of the MAPbI₃ crystallites and the AFM surface scan at 2 × 2 μm², inset in D, refers to the estimated optical bandgap of MAPbI₃).

was made in two different scanning areas, 10 × 10 and 2 × 2 μm² (inset). Large-area AFM and FE-SEM images revealed that vacuum deposition leads to dense and pinhole-free MAPbI₃ films onto a PTAA layer. Root-mean-square (RMS) roughness was calculated as 14.5 nm for a 2 × 2 μm² scan AFM area. The grain size distribution of the MAPbI₃ was determined in the range of 50–250 nm from AFM imaging, with an average of ≈150 nm. This value is slightly higher than the one derived by XRD (94 nm), which might indicate that the actual average crystallite size could be lower than the apparent grain size by AFM. Similar discrepancies were recently shown by Muscarella et al.^[68]

The optical properties of the perovskite films were examined by UV–vis spectroscopy. The typical absorbance spectrum of an evaporated MAPbI₃ film is shown in Figure 1D. The optical bandgap of the MAPbI₃ film was estimated as 1.61 eV from the Tauc plot (inset in Figure 1D) derived from its UV–vis absorption spectrum. The bandgap value of the MAPbI₃ film obtained in this study is well matched to the reported values for the tetragonal MAPbI₃ in the literature.^[69,70]

2.2. Optimization of PSCs

To evaluate the performance of the MAPbI₃ film in solar cells, we fabricated p–i–n PSCs with the following configuration: ITO/PTAA ≈10 nm/MAPbI₃ 600 nm/fullerene (C₆₀) 25 nm/bathocuproine (BCP) 7 nm/Ag 100 nm (all the layers except PTAA were

vacuum deposited). To identify the PTAA film thickness that leads to the best performance in the solar cells, a solution of PTAA in toluene (1.5 mg mL⁻¹) was spin coated on ITO substrates at different rotation speeds (1000, 3000, 5000, and 7000 rpm). The current density (*J*) versus voltage (*V*) curves of the PSCs fabricated with the PTAA layers prepared at various rotation speeds are shown in Figure 2A and the corresponding photovoltaic parameters (the best performing cell and the average of 16 cells) are shown in Table 1. A short circuit current density (*J*_{sc}) of ≈21 mA cm⁻² and an open circuit voltage (*V*_{oc}) of ≈1.10 V were observed for all cells, independently of the PTAA deposition conditions, indicating that the PTAA film completely covers the surface of the ITO at any rotation speed. In this way, the full coverage mitigates the undesirable nonradiative MAPbI₃/ITO recombination and, since all the layers are very thin independently of the rotation speed, the PTAA HTL does not impose parasitic optical absorption losses. On the other hand, the fill factor (FF) of 75.9% for the cell with PTAA prepared at 1000 rpm increased to 78.5% for a cell that had a PTAA layer processed at a rotation speed of PTAA to 7000 rpm. The small but significant increase in FF is most likely due to a decrease of the series resistance of the cells. This improvement can be explained by a thinner and more homogeneous morphology of films obtained at higher rotation speeds.

PSCs fabricated with a PTAA layer processed at 7000 rpm showed the best performance. To evaluate the reproducibility

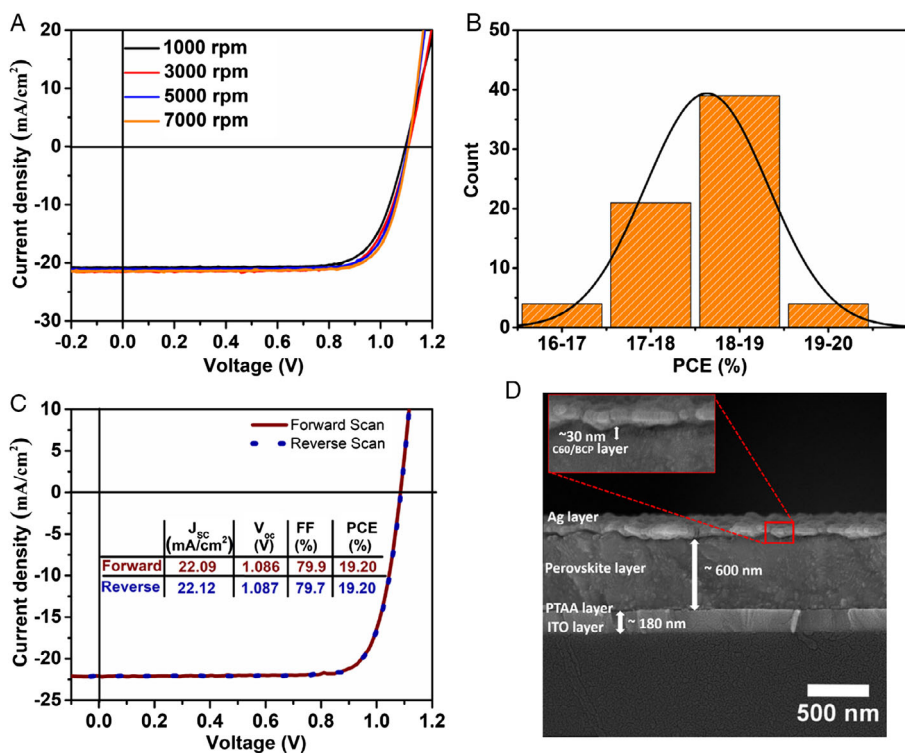


Figure 2. A) The J - V curves of the PSCs fabricated with PTAA layers prepared at various rotation speeds. B) A histogram chart of the 68 cells fabricated with PTAA layers prepared at 7000 rpm. C) J - V curves of the best performing solar cell, and D) cross-sectional FE-SEM image of a completed device. J - V curves were measured under a solar simulator at AM 1.5 G irradiation at 100 mW cm^{-2} at room temperature.

Table 1. Photovoltaic performance parameters for PSCs fabricated with PTAA prepared at different rotation speeds.

Rotation speed		J_{sc} [mA cm ⁻²]	V_{oc} [V]	FF [%]	PCE [%]
1000	Best	21.05	1.10	75.9	17.7
	Average	20.65 ± 0.46	1.098 ± 0.004	74.4 ± 1.9	17.0 ± 0.5
3000	Best	21.53	1.10	75.2	17.9
	Average	20.78 ± 0.53	1.100 ± 0.005	75.7 ± 2.8	17.3 ± 0.5
5000	Best	21.07	1.10	77.5	18.0
	Average	20.61 ± 0.50	1.097 ± 0.004	76.5 ± 2.0	17.4 ± 0.4
7000	Best	21.53	1.10	78.5	18.7
	Average	20.91 ± 0.62	1.100 ± 0.005	77.5 ± 1.2	17.9 ± 0.5

of this cell type, 68 cells were fabricated from five different batches. The histogram charts of these cells are shown in Figure 2B. The majority of the devices showed a PCE in the 18–19% range, with some surpassing 19%. Such a high reproducibility may be attributed to the vacuum-assisted thermal evaporation of almost every layer (except PTAA), as it provides a pinhole-free perovskite film (see Figure 1B,C) and allows for a fine control over the thickness of all the layers.

The J - V curves of the best performing PSC are shown in Figure 2C. The red solid and blue dotted lines represent the J - V curves in forward (from -0.2 to 1.2 V) and reverse scan (from 1.2 to -0.2), respectively. The cell exhibited a J_{sc} of

$\approx 22.09 \text{ mA cm}^{-2}$, V_{oc} of ≈ 1.086 V, FF of $\approx 79.9\%$, and overall PCE of 19.2% with negligible hysteresis.

A cross-sectional FE-SEM image of the optimum device is shown in Figure 2D. Individual layers of ITO, perovskite, C_{60}/BCP , and Ag can be distinguished with thicknesses of 180, 600, 30, and 100 nm, respectively. The thicknesses of all the vacuum-deposited layers (MAPbI_3 , C_{60}/BCP , Ag) were similar to the values that were read from the quartz crystal microbalance (QCM) sensors during the deposition.

2.3. Encapsulation

To study in detail the performance of PSCs and perovskite films, it is paramount that they are protected from ambient atmosphere. Therefore, an encapsulation method is required. We used two different methods of encapsulation that are schematically described in Figure 3. The first uses an aluminum plate and a commercial two-component epoxy adhesive, with enough space for gas exchange and film expansion inside the metal plate cap. The second method uses a low-temperature-processed ALD coating of Al_2O_3 (20 nm thick). As ALD is 3D-conformal and leads to pinhole-free films, it not only protects the outside surface of the device's top interfaces, but also fills with an Al_2O_3 coating any interstitial spaces within the layers. Therefore, the ALD encapsulation leads to a compressed stack restricting their expansion. Finally, a third encapsulation method uses the first and second methods combined.

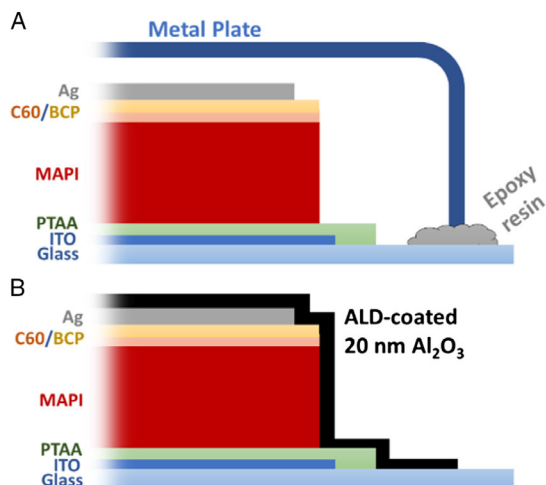


Figure 3. Scheme of the PSC encapsulation using A) an aluminum plate glued to glass with a commercial two-component epoxy adhesive resin or B) a low-temperature ALD coating of Al_2O_3 (20 nm thick).

In particular, the ALD encapsulation was done at an unusually low temperature (40°C) to ensure its compatibility with the MAPbI_3 layers. Such a low-temperature ALD process is not trivial due to use of water vapor in the process. In summary, the procedure consisted of 200 cycles of consecutive purges of TMA (10 ms)/ N_2 /water vapor (30 ms)/ N_2 , in which N_2 is also the vapor carrier for TMA and water (gas flow of 20 SCCM). At 40°C , the vapor pressure of both precursors is weak; therefore, long N_2 purges are mandatory to guarantee complete removal of the precursors from the ALD chamber when the monitored transient pressure inside the chamber returns to the chamber's baseline value (see Figure S2, Supporting Information). Failing to do so can lead to excess water, which is detrimental to the perovskite underlayer. In addition, without the complete removal of water,

chemical vapor deposition takes place, which leads to less compact, less impenetrable, and much thicker Al_2O_3 films. In the conditions and setup in our laboratory, the minimum N_2 purging times after TMA and water vapor injection were 20 and 80 s, respectively, with a growth rate of $\approx 1 \text{ \AA}$ per cycle.

This procedure was evaluated by depositing 1 and 20 nm of Al_2O_3 on top of 600 nm thick MAPbI_3 films and exposing these bilayer stacks to high temperature (150°C) in ambient conditions while monitoring its appearance and XRD patterns over time. A reference MAPbI_3 film without the ALD Al_2O_3 coating was also evaluated.

As shown in Figure 4A, heating the pristine sample leads to a loss of the original perovskite color and appearance of yellow PbI_2 -rich areas, especially at the edges. The film is almost fully converted to PbI_2 after only 3 h of heating, as corroborated by XRD data (see Figure 4B). On the other hand, the perovskite sample with 20 nm of an ALD-coated Al_2O_3 top layer maintains its original color during the time of the experiment. The sample with only 1 nm of the Al_2O_3 top layer showed decoloration but at a much slower rate than the unencapsulated perovskites. This implies that a very thin layer is already enough to slow down the MAPbI_3 decomposition. The XRD patterns of the different films are shown in Figure 4B. The diffractogram of the pristine film is also shown to facilitate the comparison (a similar pattern for a MAPbI_3 film on PTAA is described in Figure 1A). The pristine film shows the commonly observed (002) orientation of the perovskite film. The unencapsulated MAPbI_3 film is converted to PbI_2 as evidenced by the typical diffraction peak at 2θ of 12.6° . The 20 nm Al_2O_3 -coated sample also shows an increase in the PbI_2 diffraction peak and an almost complete loss of the MAPbI_3 (002) diffraction peak, which is an indication that some degradation occurs. However, surprisingly, the diffraction peak at 24.5° is significantly increased. This implies that instead of a complete degradation to PbI_2 , the perovskite crystal orientation has changed from preferentially having the (002) plane parallel to the substrate to (202). According to the XRD diffractograms in Figure S3, Supporting Information, the

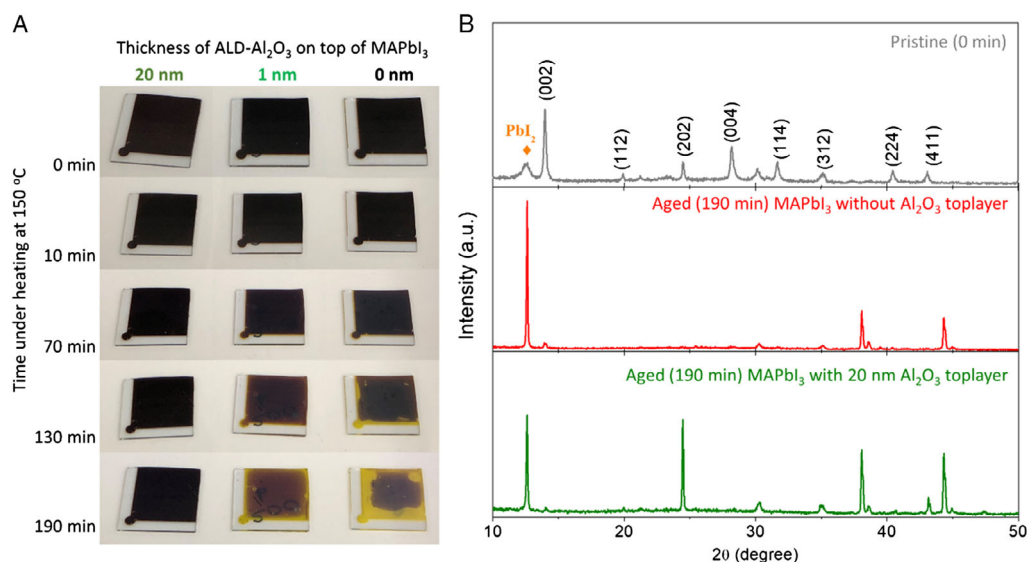


Figure 4. A) Pictures and B) XRD patterns of MAPbI_3 with and without an Al_2O_3 top layer aged at 150°C in a N_2 glovebox. The peaks around 38.5° and 44.5° in the aged samples (red and green diffractograms) are from the aluminum platform (sample holder).

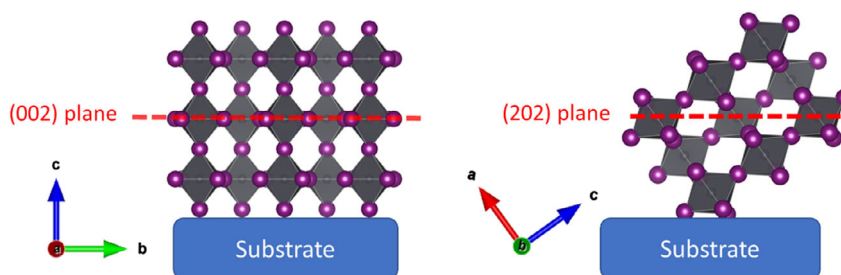


Figure 5. Schematic of the two main MAPbI₃ crystal orientations observed with respect to the substrate. Left: (002) plane parallel to substrate (*c*-axis perpendicular to the substrate). Right: (202) plane parallel to the substrate.

crystal reorientation is already observable in the first 10 min of heating; therefore, it is virtually instantaneous rather than a gradually occurring effect. In **Figure 5**, a schematic presentation of these two crystal orientations is shown. We do not understand the driving mechanism for this reorientation, but as we will explain later, it has large implications for the device stability.

2.4. Thermal Stability of the PSCs

Thermal fluctuation and especially temperature rise of the solar cell during operation can be considered the main unavoidable stress that might affect the stability of PSCs. Thermal cycling was carried out to evaluate the effect of thermal fluctuations on the PCE of the epoxy-encapsulated PSCs. For that, the encapsulated cell was cycled 200 times from 25 to 85 °C and back again to 25 °C (in ambient atmosphere). The measured *J*-*V* curves after every 50 cycles are shown in **Figure 6A** and the corresponding evolution of the photovoltaic parameters is represented in **Figure 6B**. The degradation rate of this cell is only 5% with a small drop in *V*_{oc} and *J*_{sc} after 200 cycles. This result indicates that the thermal cycles do not lead to mechanical failure or damage of any layer of the p-i-n PSC.

To evaluate the shelf life of the solar cells and the effect of the different encapsulation methods on it, the PSCs were kept at room temperature, 65 and 85 °C (on a hot plate in N₂ atmosphere) and their performance was evaluated at set intervals.

The evolution of the photovoltaic parameters for devices encapsulated with the aluminum lid and an epoxy adhesive kept at room temperature is shown in **Figure 7A**. The cells maintain ≈91% of their initial efficiency for as long as 850 h. The 6% PCE decrease occurs during the early stages, after which the PCE of the cells is stable. The drop in *J*_{sc}, FF, and *V*_{oc} was ≈6%, ≈4%, and ≈0.2%, respectively, after 850 h.

Storing the PSCs at higher temperatures induced losses in PCE over time, as shown in **Figure 7** for cells kept at 65 and at 85 °C, respectively. As we were primarily interested in evaluating the effect of prolonged heating rather than the effect of moisture on the performance of the solar cells, we performed the analysis in a nitrogen-filled glovebox. Despite this, we do see differences in performance between cells encapsulated with the different encapsulation methods.

The encapsulation using an aluminum cover with epoxy resin is less efficient in avoiding PCE losses than the ALD Al₂O₃ layer. Still, these cells retain 80% of their initial PCE (*t*₈₀) after aging for around 480 h (20 days) at 65 °C or for around 230 h (≈10 days)

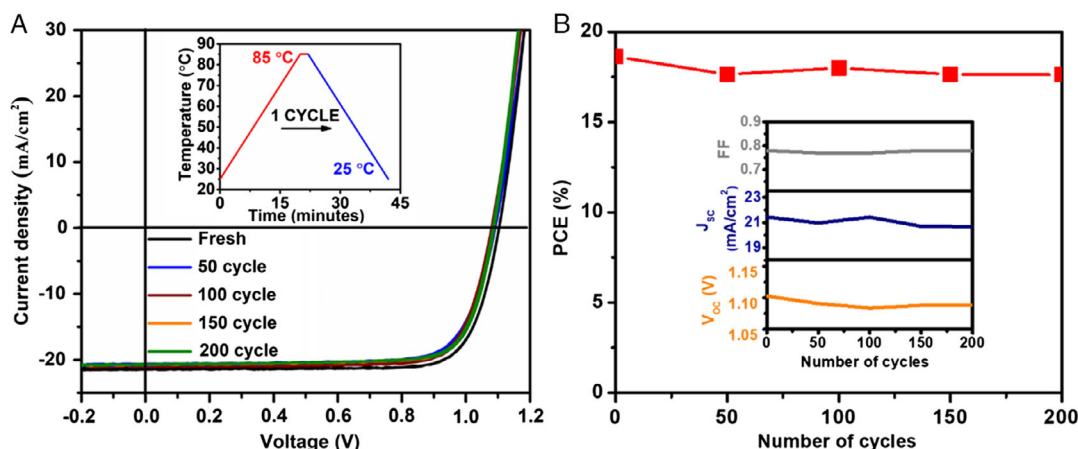


Figure 6. A) *J*-*V* curves of the devices encapsulated with the aluminum plate and epoxy adhesive after each 50 cycles between 25 and 85 °C, and B) PCE evaluation as a function of thermal cycle (the inset in (A) represents the temperature profile of one cycle and the one in (B) exhibits the loss in the other photovoltaic parameters as a function of time). *J*-*V* curves were measured in air under a solar simulator at AM 1.5 G irradiation at 100 mW cm⁻² at room temperature.

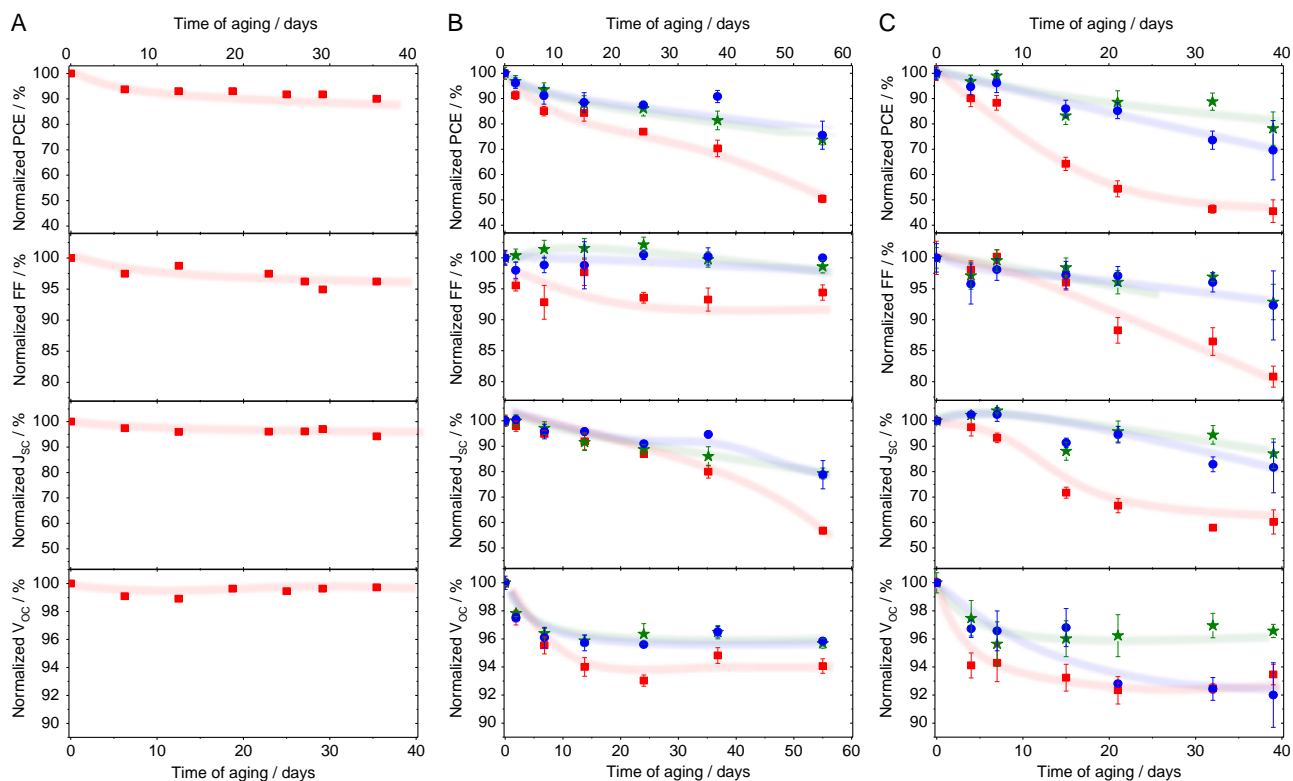


Figure 7. Evaluation of the photovoltaic parameters for ITO/PTAA/MAPbI₃/C₆₀/BCP/Ag PSCs as a function of aging time in nitrogen atmosphere at A) room temperature, B) 65 °C, and C) 85 °C, using different encapsulation methods: aluminum plate and epoxy adhesive resin (red square), ALD-coated 20 nm Al₂O₃ (green star), and a stack with both ALD and aluminum plate plus epoxy resin together (blue circle). Parameters were measured in air under a solar simulator at AM 1.5 G irradiation at 100 mW cm⁻² at room temperature.

at 85 °C. As expected, the thermal degradation is accelerated at 85 °C in comparison to 65 °C.

On the other hand, the cells encapsulated with the ALD Al₂O₃ layer are more stable even at the higher storage temperature. These have an estimated t_{80} of around 1125 h (≈47 days) and 875 h (≈37 days) at 65 and 85 °C, respectively. They gain from a more stable FF as well as less accentuated drops in both V_{oc} and J_{sc} compared to the aluminum cap encapsulation.

Finally, a combination of both encapsulation methods (with an ALD-based Al₂O₃ layer further covered with an aluminum cap with epoxy) was also evaluated. No significant differences in the evolution of the PCE was observed between the cells with this double encapsulation method and those with solely ALD Al₂O₃ coating, without a metal cap. This manifests that the ALD coating of 20 nm Al₂O₃ alone is enough to maintain a higher stability.

To understand the reasons behind the loss in efficiency, XRD measurements were conducted on the as-prepared and the aged devices (after aging for 55 days at 65 °C). The top pattern in **Figure 8** refers to the as-prepared device. In addition to the diffraction peaks of ITO, PbI₂, and tetragonal MAPbI₃ (discussed in Figure 1a), diffraction peaks ascribed to the Ag top electrode can also be observed. The whole-pattern deconvolution can be found in Figure S4, Supporting Information. The unit cell parameters (Table S3, Supporting Information) and relative peak intensities highlighting preferential orientation along the *c*-axis

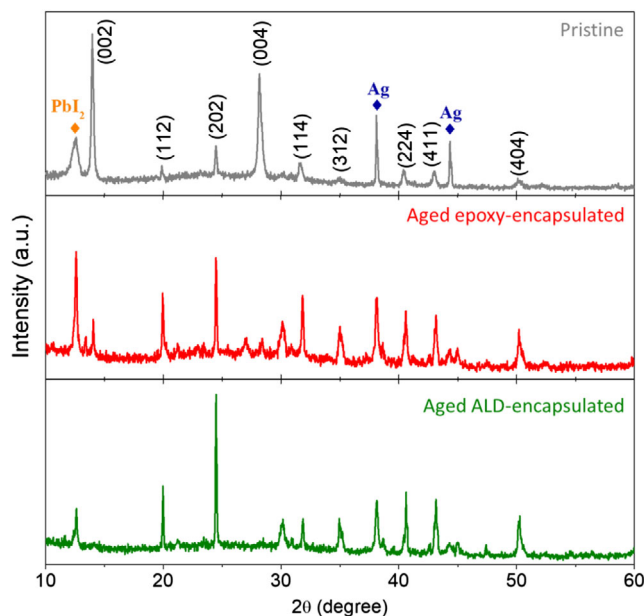


Figure 8. XRD patterns of pristine solar cells and of solar cells that were aged in N₂ atmosphere at 65 °C for 55 days having the aluminum cap plus epoxy or the ALD Al₂O₃ layer encapsulation (middle and bottom panel, respectively).

(Table S4, Supporting Information) for the as prepared device are very similar to the ones from the simple MAPbI₃ layer on ITO (Table S1 and S2, Supporting Information). This means that the further vacuum deposition of several adjacent top layers does not have a major influence on the crystallinity of the perovskite films. We only note a slightly lower average crystallite size (from 94 to 80 nm), which may be induced by radiative heating during the deposition of the metal top electrode.

The XRD diffractogram of an aluminum cap and epoxy-encapsulated device after 55 days of heating at 65 °C exhibits losses in intensity of the MAPbI₃ signals and a pronounced increase in the PbI₂ content compared to the pristine device, but with no appearance of MAI signals. This observation is in agreement with a thermal decomposition of MAPbI₃ into PbI₂, either via MAI deprotonation and subsequent sublimation of MA or even by MAI decomposition into CH₃I and NH₃ as recently observed by Shi et al.^[52] On the other hand, the XRD diffractogram of the aged ALD-Al₂O₃ layer device is not indicative of the decomposition of MAPbI₃, as the PbI₂ signal remains small, similarly to the pristine sample. This indicates that the compact, pinhole-free ALD Al₂O₃ coating can mitigate the degradation process. Probably, the compressing ALD coating seals the edges of the active layer and prevents MAI sublimation, thus disfavoring the MAI deprotonation equilibrium. However, the ALD-Al₂O₃-encapsulated solar cells present a pronounced change in crystal orientation with respect to the substrate, with a complete suppression of the original (002) signal in the diffractogram and a preferential orientation with the (202) plane parallel to the substrate. This is very similar to what was observed for the bare MAPbI₃ films encapsulated with the ALD-Al₂O₃ layer after heating at 150 °C (Figure 4). Therefore, the perovskite in an ALD-coated device preferably undergoes crystal reorientation, whereas dissociation of MAPbI₃ (with a buildup in the PbI₂ content) is the main effect observed for the epoxy one. Still, in the epoxy sample, the remaining yet-to-be-dissociated MAPbI₃ also experiences a crystal reorientation effect, although to a much lower extent.

2.5. Assessment of Operational Stability

Operational stability of the encapsulated cells was examined under continuous light soaking with maximum power point tracking (at constant room temperature and humidity). Evaluation of the PCE and the photovoltaic parameters as a function of time is displayed in Figure 9, showing that the performance of all samples decreases continuously. Although the Al₂O₃ is the more stable one, no significant changes are observed in the operational *t*₈₀ of epoxy- and ALD-encapsulated samples (≈240 and 270 h, respectively).

After 250 h under continuous illumination at maximum power point tracking (MPPT), the XRD signals (see Figure 10) of the MAPbI₃ diffraction peaks are much less intense relative to those of the Ag and PbI₂ peaks (the whole-pattern deconvolution can be found in Figure S5, Supporting Information, the relative peak intensities highlighting preferential orientation along the c-axis in Table S5, Supporting Information, and the unit cell parameters in Table S6, Supporting information). This reduction in peak intensity is indicative of an amorphization effect of the perovskite. As the grain boundaries are the typical amorphous regions of a

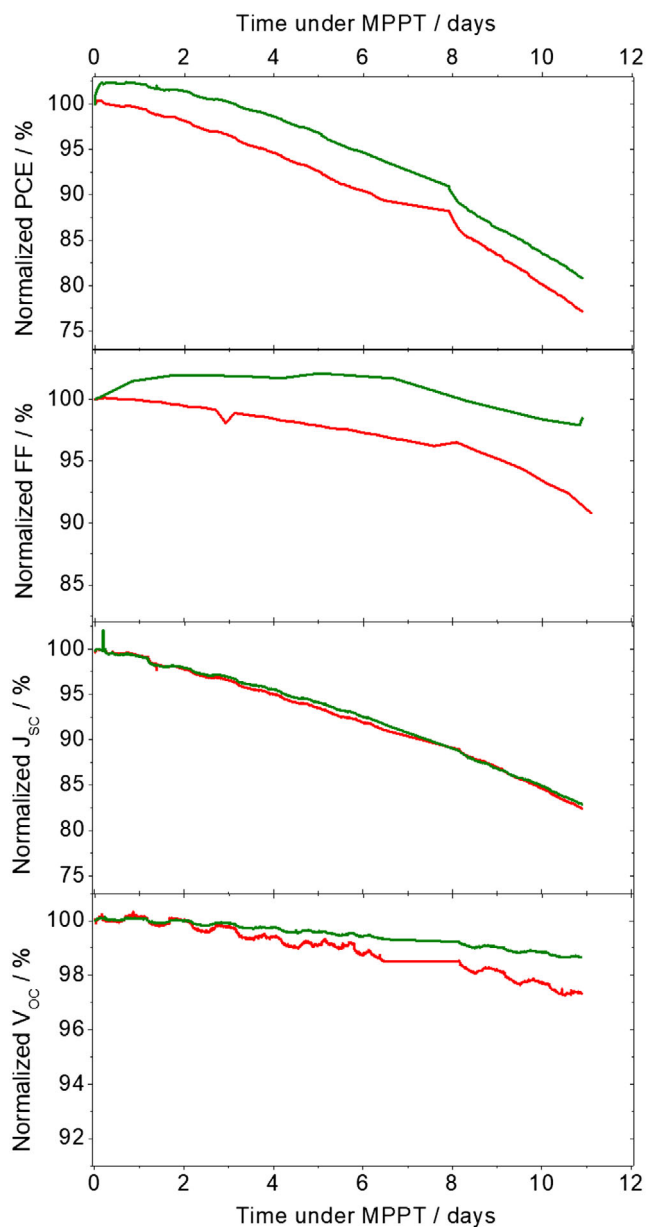


Figure 9. Evaluation of the PCE as a function of time under continuous light soaking at MPPT using different encapsulation methods: epoxy adhesive resin (red line) and ALD-coated 20 nm Al₂O₃ (green line). Parameters were measured in a N₂-filled chamber under a white LED light source (1 sun equivalent) at 30 °C.

polycrystalline thin film, it is expected that such an amorphization is the result of a decrease in crystallite sizes. From our fit we do observe this, with an average crystallite size of 80 nm in the pristine film to 64 nm for the film that was operated under MPPT. Also, here we see that the relative intensity of the (202) to the (002) orientation is strongly increased after operation under MPP. This implies that similarly to the case of thermal stress a reorientation of the crystals is taking place that coincides with the loss in solar cell performance.

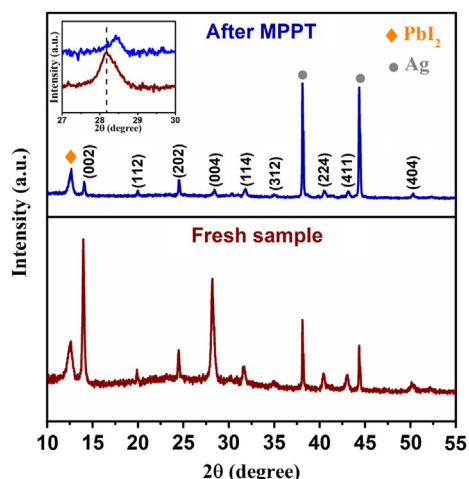


Figure 10. XRD patterns of fresh and MPPT-aged devices.

In addition, compressive stress is also observed on the MAPbI₃ crystallites, as evidenced by a shift of diffraction peaks to higher angles (inset in Figure 10 shows an example for the (004) peak). This is observed for all diffraction peaks from MAPbI₃, but not for ITO, evidencing that this is not an instrumental artifact. As a result, all cell parameters are found to decrease, leading to a slight shrinkage of the unit cell volume from 996 to 984 Å³ (see Table S6, Supporting Information). This compressive stress is consistent with the aforementioned partial amorphization of the perovskite. Indeed, amorphous phases generally have lower density (due to expansion to higher specific volume) than crystalline phases. However, such expansion is restricted for evaporated layers in a compact sandwiched architecture, and even more with the ALD coating. In this case, the observed partial amorphization eventually resulted in a compression of the remaining crystalline phase, to maintain an identical total volume.

To shed more light on the recombination mechanism after operational aging, the V_{OC} and FF of freshly fabricated and MPPT-aged PSCs were measured as a function of light intensity (Figure 11A,B). The ideality factors of the cells were calculated

(from the slope of the V_{OC} versus logarithmic light intensity plot) as 1.4 for the fresh cell and 2.0 for the aged one. The larger ideality factor can be a consequence of increased trap-assisted (Shockley–Read–Hall) recombination after MPPT aging.^[71,72] This hypothesis is also supported by the trend of the FF when decreasing the light intensity (carrier concentration). In the as-prepared cells, the FF shows a moderate increase to values as high as 80.7 at low light intensity, which is expected as fewer charge carriers are generated and can be more efficiently extracted. The increase is small, however, indicating that charge trapping is already present to some extent in as-prepared devices. The trend is very different in aged cells, where the FF systematically diminishes with decreasing light intensity. In other words, at low carrier concentration the charge transport/extraction becomes less efficient, which indicates the presence of a large density of trap states. Therefore, the intensity dependence of V_{OC} and FF supports that trap-assisted recombination is the dominating mechanism in aged cells,^[73] a consequence of the structural changes and in particular of the crystal reorientation (as observed by XRD).

In summary, we studied the effect of thermal stress and light soaking in p–i–n PSCs with PCEs exceeding 19%, using dopant-free PTAA as the HTL and coevaporated MAPbI₃ (and adjacent ETLs). On PTAA, the vacuum-deposited MAPbI₃ layer grows as a dense and pinhole-free polycrystalline film, in a tetragonal structure, and with the *c*-axis preferentially oriented perpendicular to the substrate. The corresponding solar cells exhibit outstanding thermal cycling stability, with a small PCE drop of only 5% even after 200 cycles between 25 and 85 °C. A low-temperature (40 °C) ALD-Al₂O₃ coating was developed and used to protect the MAPbI₃ layers and the solar cells from environmental agents. This method can be extended to any device or material that requires mild processing conditions. The ALD coating leads to improved thermal stability, maintaining 80% of the initial PCEs after aging for ≈40 and 37 days at 65 and 85 °C, respectively. This is among the largest stability reported for coevaporated MAPbI₃-based p–i–n PSCs. Importantly, room-temperature operation of the solar cells under 1 sun illumination leads to t_{80} of ≈10 days of continuous operation at MPPT. Even though this is satisfactory for

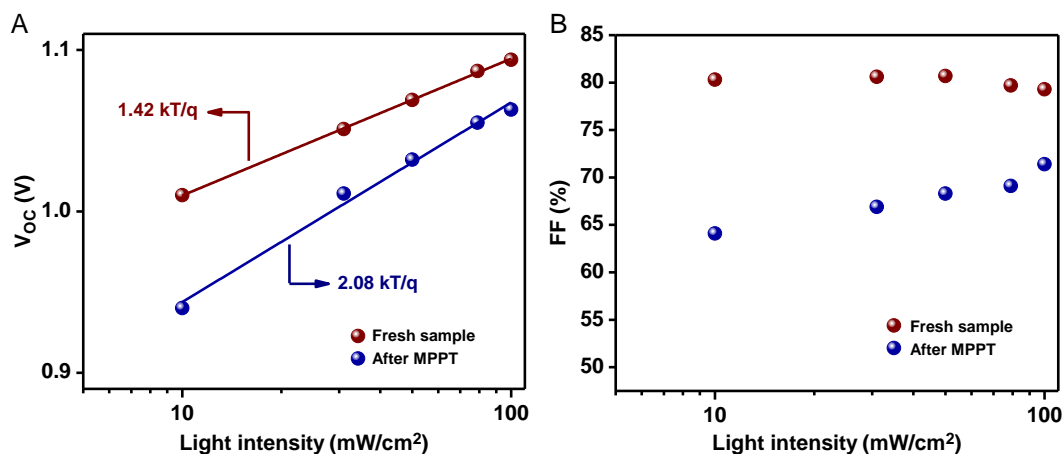


Figure 11. Light dependence of A) V_{OC} and B) FF as a function of logarithmic light intensity of fresh and MPPT-aged devices. Parameters were measured in air under a solar simulator at AM 1.5 G irradiation at 100 mW cm⁻² at room temperature.

MAPbI₃-based p–i–n PSCs, it is significantly shorter than the shelf lifetime at elevated temperature. Thanks to the rigorous encapsulation, such decrease in operational stability is not caused by the chemical degradation of the perovskite film to its precursors (PbI₂, MAI), but rather by a change in crystal orientation of the perovskite. This effect occurs also with temperature, but it is accelerated under intense illumination. It appears that the structural change results in a larger density of trap states, which reduces all key performance parameters of the solar cells, most notably the current density. This is an important finding, which should be taken into account in the development of more stable perovskite absorbers, for example, by stabilization of the material orientation through judicious choice of substrate, as well as of the deposition conditions.

3. Experimental Section

Materials: Photolithographically patterned ITO-coated glass substrates were purchased from Naranjo Substrates. C₆₀ and PTAA were provided by Sigma Aldrich. PbI₂, CH₃NH₃I (MAI), and BCP were purchased from Lumtec.

Device Fabrication and Encapsulation: Prior to the fabrication of the cell, photolithographically patterned ITO-coated glass substrates were cleaned sequentially in soapy water, deionized water, and isopropanol for 10 min in an ultrasonic bath, followed by UV-ozone treatment for 20 min. Then, to explore the effect of the rotation speed on the photovoltaic performance of the cells, PTAA solution (1.5 mg mL⁻¹ in toluene) was spin coated at 1000, 3000, 5000, and 7000 rpm for 30 s and annealed at 100 °C for 10 min. After the substrates cooled to room temperature, PTAA-coated substrates were transferred to a vacuum chamber integrated into a nitrogen-filled glovebox to evaporate MAPbI₃, C₆₀, and BCP layers. Two evaporation sources (one for PbI₂ and one for MAI) and three QCM sensors were used for MAPbI₃ deposition. While two sensors were used to monitor the deposition rate of the sources, the total deposition rate was followed by the third one close to the substrate holder. When the pressure in the vacuum chamber reached 3×10^{-6} mbar, the sources were heated to ≈ 80 °C for MAI and ≈ 290 °C for PbI₂. During the coevaporation process, the rates of the PbI₂ and MAI were 0.6 and 1 Å s⁻¹, respectively. After the deposition of the 600 nm MAPbI₃ film, the chamber was vented to replace PbI₂ and MAI crucibles with those containing C₆₀ and BCP. First, the C₆₀ layer with a thickness of 25 nm was deposited at 0.5 Å s⁻¹, and then a 7 nm thick BCP layer was sublimed at 0.3 Å s⁻¹ without breaking the vacuum. Finally, to complete the device, 100 nm of Ag as a top metal contact was deposited in a second vacuum chamber.

For devices encapsulated with epoxy resin, a commercial Araldite two-component epoxy resin (2014-2) was spread at the edges of a square 4.8 cm² aluminum plate, with bent edges of 1 mm height, then centered at the device substrate fully covering the MAPbI₃ film area inside the resin/aluminum perimeter. The resin was cured in glovebox for minimum 3 h.

For devices encapsulated by ALD coating, a Arradiance's GEMStar XT Thermal ALD system integrated into a nitrogen-filled glovebox was used. The ALD chamber was heated to 40 °C, while the precursor and oxidizer manifolds (to which the bottles of TMA and water were connected) were heated to 115 and 140 °C, respectively, to avoid vapor accumulation at the tubes leading to the main chamber. Prior to deposition, the tubes and valves were degassed three times by performing pulses with the bottles manually closed, to avoid contamination. The edges of the ITO and AG contacts of the devices were protected with Dupont's polyimide Kapton tape and the substrates were inserted in the chamber, which was then evacuated. A N₂ gas flow of 20 SCCP was used as TMA and water vapor carrier. A cycle consisted of consecutive purges of TMA for 10 ms and water vapor for 30 ms, each followed by N₂ purges for enough time to guarantee complete removal of the precursors from the ALD chamber, as monitored by the transient pressure inside the chamber (see Figure S2, Supporting Information).

Characterization: The crystalline structure of the MAPbI₃ films was characterized by XRD using an Empyrean PANalytical diffractometer operating at 45 kV and 40 mA. Measurements were taken in the Bragg-Brentano geometry using Cu K α ($\lambda = 1.54$ Å) radiation. Diffraction patterns were recorded from 10° to 60° at room temperature with a step size of 0.03°. The microstructure of the samples was investigated using a Hitachi S-4800 FE-SEM. The surface morphology of the films was analyzed using AFM (Multimode SPM, Veeco, USA). The optical properties of the films were investigated using a fiber optics based Avantes Avaspec2048 Spectrometer.

The current density–voltage (*J*–*V*) characteristics were obtained using a Keithley 2612 A source measure unit under simulated AM 1.5 G irradiation at 100 mW cm⁻² (xenon lamp, Abet Technologies model 10 500) outside the glovebox. Before each measurement, the exact light intensity was determined using a calibrated Si reference diode. The *J*–*V* curves were recorded between –0.2 and 1.2 V with 0.01 V steps. The layout used to test the solar cells had 16 equal areas (0.0825 cm²) and was measured through a shadow mask with 0.05 cm². Light intensity dependence measurements were done by placing neutral density filters (LOT-QuantumDesign GmbH) between the light source and the device. For the shelf stability experiments (room temperature, 65 and 85 °C), devices were aged in a glovebox using a hot plate and the *J*–*V* curves were measured outside the glovebox. Thermal cycling was conducted between 25 and 85 °C in a Heraeus (HT 4002) temperature cycling furnace. The *J*–*V* curve of the cells was measured after each 50 cycles. For the operational stability tests, photovoltaic parameters of the cells in the N₂ filled chamber were tracked at MPP condition with a white LED light source under 1 sun equivalent (developed by candlelight). The temperature was stabilized at ≈ 30 °C during the entire measurement using a water-circulating cooling system controlled by a Peltier element.

Supporting Information

Supporting Information is available from the Wiley Online Library or from the author.

Acknowledgements

The research leading to these results received funding from the European Research Council (ERC) under the European Union's Horizon 2020 research and innovation program (grant agreement no. 834431) and the Spanish Ministry of Science, Innovation and Universities (MICIU, MAT2017-88821-R, RTI2018-095362-A-I00, PCI2019-111829-2, and EQC2018-004888-P) and the Comunitat Valenciana (IDIFEDER/2018/061 and Prometeu/2020/077). M.S. and F.P. acknowledge the MICIU for their RyC and JdC contracts, respectively. I.C.K. would like to thank TUBITAK 2214-A – International Doctoral Research Fellowship Programme for supporting his research at ICMol.

Conflict of Interest

The authors declare no conflict of interest.

Keywords

atomic layer deposition, crystal orientation, perovskite solar cells, stability, thermal evaporation

Received: November 3, 2020

Revised: December 6, 2020

Published online: January 14, 2021

- [1] A. Kojima, K. Teshima, Y. Shirai, T. Miyasaka, *J. Am. Chem. Soc.* **2009**, *131*, 6050.
- [2] A. K. Jena, A. Kulkarni, T. Miyasaka, *Chem. Rev.* **2019**, *119*, 3036.
- [3] S. Akin, F. Sadegh, S. Turan, S. Sonmezoglu, *ACS Appl. Mater. Interfaces* **2019**, *11*, 45142.
- [4] C. Momblona, L. Gil-Escrig, E. Bandiello, E. M. Hutter, M. Sessolo, K. Lederer, J. Blochwitz-Nimoth, H. J. Bolink, *Energy Environ. Sci.* **2016**, *9*, 3456.
- [5] S. Akin, Y. Liu, M. I. Dar, S. M. Zakeeruddin, M. Grätzel, S. Turan, S. Sonmezoglu, *J. Mater. Chem. A* **2018**, *6*, 20327.
- [6] X. Zheng, Y. Hou, C. Bao, J. Yin, F. Yuan, Z. Huang, K. Song, J. Liu, J. Troughton, N. Gasparini, C. Zhou, Y. Lin, D.-J. Xue, B. Chen, A. K. Johnston, N. Wei, M. N. Hedhili, M. Wei, A. Y. Alsalloum, P. Maity, B. Turedi, C. Yang, D. Baran, T. D. Anthopoulos, Y. Han, Z.-H. Lu, O. F. Mohammed, F. Gao, E. H. Sargent, O. M. Bakr, *Nat. Energy* **2020**, *5*, 131.
- [7] H. Min, M. Kim, S. U. Lee, H. Kim, G. Kim, K. Choi, J. H. Lee, S. Il Seok, *Science* **2019**, *366*, 749.
- [8] E. H. Jung, N. J. Jeon, E. Y. Park, C. S. Moon, T. J. Shin, T. Y. Yang, J. H. Noh, J. Seo, *Nature* **2019**, *567*, 511.
- [9] P. Holzhey, M. Saliba, *J. Mater. Chem. A* **2018**, *6*, 21794.
- [10] Y.-H. Lin, N. Sakai, P. Da, J. Wu, H. C. Sansom, A. J. Ramadan, S. Mahesh, J. Liu, R. D. J. Oliver, J. Lim, L. Aspitarte, K. Sharma, P. K. Madhu, A. B. Morales-Vilches, P. K. Nayak, S. Bai, F. Gao, C. R. M. Grovenor, M. B. Johnston, J. G. Labram, J. R. Durrant, J. M. Ball, B. Wenger, B. Stannowski, H. J. Snaith, *Science* **2020**, *369*, 96.
- [11] T. T. Ava, A. Al Mamun, S. Marsillac, G. Namkoong, *Appl. Sci.* **2019**, *9*, 188.
- [12] M. V. Khenkin, E. A. Katz, A. Abate, G. Bardizza, J. J. Berry, C. Brabec, F. Brunetti, V. Bulović, Q. Burlingame, A. Di Carlo, R. Cheacharoen, Y.-B. Cheng, A. Colmann, S. Cros, K. Domanski, M. Dusza, C. J. Fell, S. R. Forrest, Y. Galagan, D. Di Girolamo, M. Grätzel, A. Hagfeldt, E. von Hauff, H. Hoppe, J. Kettle, H. Köbler, M. S. Leite, S. Liu, Y.-L. Loo, J. M. Luther, et al., *Nat. Energy* **2020**, *5*, 35.
- [13] Z. Liu, L. Qiu, L. K. Ono, S. He, Z. Hu, M. Jiang, G. Tong, Z. Wu, Y. Jiang, D.-Y. Son, Y. Dang, S. Kazaoui, Y. Qi, *Nat. Energy* **2020**, *5*, 596.
- [14] B. Conings, J. Drikkonigen, N. Gauquelin, A. Babayigit, J. D'Haen, L. D'Olieslaeger, A. Ethirajan, J. Verbeeck, J. Manca, E. Mosconi, F. De Angelis, H.-G. Boyen, *Adv. Energy Mater.* **2015**, *5*, 1500477.
- [15] Y.-H. Chiang, M. Anaya, S. D. Stranks, *ACS Energy Lett.* **2020**, *5*, 2498.
- [16] P. Holzhey, P. Yadav, S.-H. Turren-Cruz, A. Ummadisingu, M. Grätzel, A. Hagfeldt, M. Saliba, *Mater. Today* **2019**, *29*, 10.
- [17] A. E. Williams, P. J. Holliman, M. J. Carnie, M. L. Davies, D. A. Worsley, T. M. Watson, *J. Mater. Chem. A* **2014**, *2*, 19338.
- [18] F. Palazon, D. Perez-Del-Rey, B. Danekamp, C. Dreessen, M. Sessolo, P. P. Boix, H. J. Bolink, *Adv. Mater.* **2019**, *31*, e1902692.
- [19] C.-H. Chiang, C.-G. Wu, *ChemSusChem* **2016**, *9*, 2666.
- [20] F. Wang, S. Bai, W. Tress, A. Hagfeldt, F. Gao, *NPJ Flexi. Electron.* **2018**, *2*, 22.
- [21] J. Borchert, I. Levchuk, L. C. Snoek, M. U. Rothmann, R. Haver, H. J. Snaith, C. J. Brabec, L. M. Herz, M. B. Johnston, *ACS Appl. Mater. Interfaces* **2019**, *11*, 28851.
- [22] Z. Safari, M. B. Zarandi, M. R. Nateghi, *Chem. Pap.* **2019**, *73*, 2667.
- [23] J. Kim, B. Park, J. Baek, J. S. Yun, H.-W. Kwon, J. Seidel, H. Min, S. Coelho, S. Lim, S. Huang, K. Gaus, M. A. Green, T. J. Shin, A. W. Y. Ho-Baillie, M. G. Kim, S. Il Seok, *J. Am. Chem. Soc.* **2020**, *142*, 6251.
- [24] M. Xiao, F. Huang, W. Huang, Y. Dkhissi, Y. Zhu, J. Etheridge, A. Gray-Weale, U. Bach, Y. B. Cheng, L. Spiccia, *Angew. Chem. Int. Ed.* **2014**, *53*, 9898.
- [25] A. T. Barrows, A. J. Pearson, C. K. Kwak, A. D. F. Dunbar, A. R. Buckley, D. G. Lidzey, *Energy Environ. Sci.* **2014**, *7*, 2944.
- [26] M. Adnan, J. K. Lee, *RSC Adv.* **2020**, *10*, 5454.
- [27] Y. Deng, E. Peng, Y. Shao, Z. Xiao, Q. Dong, J. Huang, *Energy Environ. Sci.* **2015**, *8*, 1544.
- [28] M. Liu, M. B. Johnston, H. J. Snaith, *Nature* **2013**, *501*, 395.
- [29] O. Malinkiewicz, A. Yella, Y. H. Lee, G. M. M. Espallargas, M. Graetzel, M. K. Nazeeruddin, H. J. Bolink, *Nat. Photonics* **2014**, *8*, 128.
- [30] L. K. Ono, M. R. Leyden, S. Wang, Y. Qi, *J. Mater. Chem. A* **2016**, *4*, 6693.
- [31] J. Ávila, C. Momblona, P. P. Boix, M. Sessolo, H. J. Bolink, *Joule* **2017**, *1*, 431.
- [32] J. Li, H. Wang, X. Y. Chin, H. A. Dewi, K. Vergeer, T. W. Goh, J. W. M. Lim, J. H. Lew, K. P. Loh, C. Soci, T. C. Sum, H. J. Bolink, N. Mathews, S. Mhaisalkar, A. Bruno, *Joule* **2020**, *4*, 1035.
- [33] A. D. Wright, C. Verdi, R. L. Milot, G. E. Eperon, M. A. Perez-Osorio, H. J. Snaith, F. Giustino, M. B. Johnston, L. M. Herz, *Nat. Commun.* **2016**, *7*.
- [34] J. Borchert, R. L. Milot, J. B. Patel, C. L. Davies, A. D. Wright, L. Martínez Maestro, H. J. Snaith, L. M. Herz, M. B. Johnston, *ACS Energy Lett.* **2017**, *2*, 2799.
- [35] J. Avila, L. Gil-Escrig, P. P. Boix, M. Sessolo, S. Albrecht, H. J. Bolink, *Sustain. Energy Fuels* **2018**, *2*, 2429.
- [36] Q. Ma, S. Huang, X. Wen, M. A. Green, A. W. Y. Ho-Baillie, *Adv. Energy Mater.* **2016**, *6*, 1502202.
- [37] D. Akin Kara, K. Kara, G. Oylumluoglu, M. Z. Yigit, M. Can, J. J. Kim, E. K. Burnett, D. L. Gonzalez Arellano, S. Buyukcelebi, F. Ozel, O. Usluer, A. L. Briseno, M. Kus, *ACS Appl. Mater. Interfaces* **2018**, *10*, 30000.
- [38] K. Choi, H. Choi, J. Min, T. Kim, D. Kim, S. Y. Son, G.-W. Kim, J. Choi, T. Park, *Sol. RRL* **2020**, *4*, 1900251.
- [39] L. Meng, J. You, T.-F. Guo, Y. Yang, *Acc. Chem. Res.* **2016**, *49*, 155.
- [40] M. Roß, L. Gil-Escrig, A. Al-Ashouri, P. Tockhorn, M. Joßt, B. Rech, S. Albrecht, *ACS Appl. Mater. Interfaces* **2020**, *12*, 39261.
- [41] Q. Zhao, R. Wu, Z. Zhang, J. Xiong, Z. He, B. Fan, Z. Dai, B. Yang, X. Xue, P. Cai, S. Zhan, X. Zhang, J. Zhang, *Org. Electron.* **2019**, *71*, 106.
- [42] M. Stolterfoht, C. M. Wolff, Y. Amir, A. Paulke, L. Perdigón-Toro, F. Caprioglio, D. Neher, *Energy Environ. Sci.* **2017**, *10*, 1530.
- [43] Z. Liu, L. Krückemeier, B. Krogmeier, B. Klingebiel, J. A. Márquez, S. Levchenko, S. Öz, S. Mathur, U. Rau, T. Unold, T. Kirchartz, *ACS Energy Lett.* **2019**, *4*, 110.
- [44] A. G. Boldyreva, I. S. Zhidkov, S. Tsarev, A. F. Akbulatov, M. M. Tepliakova, Y. S. Fedotov, S. I. Bredikhin, E. Y. Postnova, S. Y. Luchkin, E. Z. Kurmaev, K. J. Stevenson, P. A. Troshin, *ACS Appl. Mater. Interfaces* **2020**, *12*, 19161.
- [45] L. Meng, J. You, Y. Yang, *Nat. Commun.* **2018**, *9*, 5265.
- [46] F. J. Ramos, T. Maindron, S. Béchu, A. Rebai, M. Frégnaux, M. Bouttermy, J. Rousset, P. Schulz, N. Schneider, *Sustain. Energy Fuels* **2018**, *2*, 2468.
- [47] R. Cheacharoen, N. Rolston, D. Harwood, K. A. Bush, R. H. Dauskardt, M. D. McGehee, *Energy Environ. Sci.* **2018**, *11*, 144.
- [48] D. B. Khadka, Y. Shirai, M. Yanagida, K. Miyano, *J. Mater. Chem. C* **2018**, *6*, 162.
- [49] F. Matteocci, L. Cinà, E. Lamanna, S. Cacovich, G. Divitini, P. A. Midgley, C. Ducati, A. Di Carlo, *Nano Energy* **2016**, *30*, 162.
- [50] F. Bella, G. Griffini, J.-P. Correa-Baena, G. Saracco, M. Grätzel, A. Hagfeldt, S. Turri, C. Gerbaldi, *Science* **2016**, *354*, 203.
- [51] H. C. Weerasinghe, Y. Dkhissi, A. D. Scully, R. A. Caruso, Y.-B. Cheng, *Nano Energy* **2015**, *18*, 118.

- [52] L. Shi, M. P. Bucknall, T. L. Young, M. Zhang, L. Hu, J. Bing, D. S. Lee, J. Kim, T. Wu, N. Takamure, D. R. McKenzie, S. Huang, M. A. Green, A. W. Y. Ho-Baillie, *Science* **2020**, *368*, eaba2412.
- [53] L. Shi, T. L. Young, J. Kim, Y. Sheng, L. Wang, Y. Chen, Z. Feng, M. J. Keevers, X. Hao, P. J. Verlinden, M. A. Green, A. W. Y. Ho-Baillie, *ACS Appl. Mater. Interfaces* **2017**, *9*, 25073.
- [54] S. Lee, J.-H. Han, S.-H. Lee, G.-H. Baek, J.-S. Park, *JOM* **2019**, *71*, 197.
- [55] R. W. Johnson, A. Hultqvist, S. F. Bent, *Mater. Today* **2014**, *17*, 236.
- [56] V. Zardetto, B. L. Williams, A. Perrotta, F. Di Giacomo, M. A. Verheijen, R. Andriessen, W. M. M. Kessels, M. Creatore, *Sustain. Energy Fuels* **2017**, *1*, 30.
- [57] C.-Y. Chang, K.-T. Lee, W.-K. Huang, H.-Y. Siao, Y.-C. Chang, *Chem. Mater.* **2015**, *27*, 5122.
- [58] Y. Il Lee, N. J. Jeon, B. J. Kim, H. Shim, T.-Y. Yang, S. Il Seok, J. Seo, S. G. Im, *Adv. Energy Mater.* **2018**, *8*, 1701928.
- [59] I. S. Kim, A. B. F. Martinson, *J. Mater. Chem. A* **2015**, *3*, 20092.
- [60] R. Singh, S. Ghosh, A. S. Subbiah, N. Mahuli, S. K. Sarkar, *Sol. Energy Mater. Sol. Cells* **2020**, *205*, 110289.
- [61] Y. Lv, P. Xu, G. Ren, F. Chen, H. Nan, R. Liu, D. Wang, X. Tan, X. Liu, H. Zhang, Z.-K. Chen, *ACS Appl. Mater. Interfaces* **2018**, *10*, 23928.
- [62] Z. Hu, Z. Liu, L. K. Ono, M. Jiang, S. He, D.-Y. Son, Y. Qi, *Adv. Energy Mater.* **2020**, *10*, 2000908.
- [63] D. Pérez-del-Rey, L. Gil-Escrig, K. P. S. Zanoni, C. Dreessen, M. Sessolo, P. P. Boix, H. J. Bolink, *Chem. Mater.* **2019**, *31*, 6945.
- [64] C. Roldán-Carmona, P. Gratia, I. Zimmermann, G. Grancini, P. Gao, M. Graetzel, M. K. Nazeeruddin, *Energy Environ. Sci.* **2015**, *8*, 3550.
- [65] M. Szafranski, A. Katrusiak, *J. Phys. Chem. Lett.* **2016**, *7*, 3458.
- [66] J. Borchert, H. Boht, W. Fränzel, R. Csuk, R. Scheer, P. Pistor, *J. Mater. Chem. A* **2015**, *3*, 19842.
- [67] S. Kavadiya, J. Strzalka, D. M. Niedzwiedzki, P. Biswas, *J. Mater. Chem. A* **2019**, *7*, 12790.
- [68] L. A. Muscarella, E. M. Hutter, S. Sanchez, C. D. Dieleman, T. J. Savenije, A. Hagfeldt, M. Saliba, B. Ehrler, *J. Phys. Chem. Lett.* **2019**, *10*, 6010.
- [69] Y. Kumar, E. Regalado-Pérez, A. M. Ayala, N. R. Mathews, X. Mathew, *Sol. Energy Mater. Sol. Cells* **2016**, *157*, 10.
- [70] T. Jesper Jacobsson, J.-P. Correa-Baena, M. Pazoki, M. Saliba, K. Schenk, M. Grätzel, A. Hagfeldt, *Energy Environ. Sci.* **2016**, *9*, 1706.
- [71] G.-J. A. H. Wetzelaer, M. Scheepers, A. M. Sempere, C. Momblona, J. Ávila, H. J. Bolink, *Adv. Mater.* **2015**, *27*, 1837.
- [72] C. M. Wolff, P. Caprioglio, M. Stolterfoht, D. Neher, *Adv. Mater.* **2019**, *31*, 1902762.
- [73] T. S. Sherkar, C. Momblona, L. Gil-Escrig, J. Ávila, M. Sessolo, H. J. Bolink, L. J. A. Koster, *ACS Energy Lett.* **2017**, *2*, 1214.